Research Article Vol. 42, No. 12 / December 2025 / Journal of the Optical Society of America B 2747

Journal of the Optical Society of America B

OPTICAL PHYSICS

Phase matching in vector beam-driven high-harmonic generation with 3D-printed gas cells

D. Attiyah,[1,*] H. Allison,[1] J. To,[1] P. G. Kazansky,[2] D. Schmidt,[3] C. Gardner,[1] V. Flores,[1] J. Lewis,[1] C. G. Durfee,[3] and F. Dollar[1]

[1]STROBE, NSF Science & Technology Center, University of California, Irvine, Irvine, California 92697, USA
[2]Optoelectronics Research Centre, University of Southampton, Southampton, UK
[3]Department of Physics, Colorado School of Mines, Golden, Colorado 80401, USA
*dattiyah@uci.edu

Received 16 July 2025; revised 7 October 2025; accepted 12 October 2025; posted 27 October 2025; published 13 November 2025

We present experimental results of high-harmonic generation (HHG) driven by a 1300 nm beam in three different polarization states: linear, radial, and azimuthal. We found that the optimal pressure for phase matching was roughly twice as high for the vector beam drivers than the linear driver. We attribute this difference in pressure primarily to the Gouy phase, which differs by a factor of two between the linear and vector polarization states. We demonstrate a target for HHG that produces a uniform pressure profile in the interaction region that is nearly identical to the backing pressure and preserves the mode of the driving beam. We provide characterization and validation of this technique through flow simulations and experimental measurements.

https://doi.org/10.1364/JOSAB.572118

1. INTRODUCTION

Vector beams, or laser beams with spatially dependent polarization, have garnered interest across many disciplines in recent years. A common example is the radially polarized beam, which is locally linearly polarized at each point in space but with a macroscopic polarization state that points away from the beam center. At the center, the superposition of these varying polarization vectors creates a singularity, resulting in a characteristic ring-shaped intensity profile. The orthogonality and tight focusing capabilities [1] of these vector beams have enabled advances in optical communications [2–5], microscopy [6–8], and optical tweezers [9–13]. These same properties have also expanded the capabilities of ultrafast lasers, or lasers with full-width at half-maximum (FWHM) pulse durations of <100 femtoseconds (10^{-15} s), in applications such as materials processing [14–17], magnetic probing for materials research [18,19], and laser-driven particle acceleration [20,21].

High harmonic generation (HHG) is a nonlinear, frequency upconverting process that produces harmonic radiation, or light with wavelengths at integer multiples of the driving beam. When driven by near-infrared (NIR) ultrafast beams, this interaction can produce light in the extreme ultraviolet (EUV) wavelength range with pulse durations on the attosecond (10^{-18} s) scale [22–24]. The microscopic physics of HHG is often described by a semi-classical three-step recombination model [25], consisting of tunnel ionization of the electron, acceleration by the laser field, and recombination with the parent atom accompanied by the emission of the upconverted photon [26]. When the driving laser has a longer wavelength, the electron is accelerated for a longer period of time, causing it to gain more energy and release a higher-energy photon upon recombination. Therefore, driving beams with longer wavelengths are capable of producing higher-energy, or shorter-wavelength, photons [27,28]. The emitted spectrum from a single atom would appear as a plateau across the relevant wavelengths.

Phase matching describes the macroscopic coherent buildup of harmonic radiation in the interacting medium by the minimization of the phase mismatch between the driving beam and the harmonic beam. The flux of the harmonic beam acquires a Gaussian-like shape and can be significantly increased when phase-matching conditions are met [29]. The total phase mismatch between the driving field and a given harmonic order can be written as a sum of the dominant sources of dispersion [30]: $\Delta k = \Delta k_{\text{plasma}} + \Delta k_{\text{neutral}} + \Delta k_{\text{Gouy}} + \Delta k_{\text{intrinsic}}$, where the right-hand side represents the phase mismatch due to propagation in plasma and neutral gas [31], focusing geometry [32], and the intrinsic nonlinear phase [33–36], respectively. These terms depend on target parameters such as ionization potential and density profile, as well as laser properties, including intensity, wavelength, polarization, and mode [37–39]. Phase matching

at longer wavelengths has been demonstrated across the mid-infrared wavelength region, where higher densities were used to reach suitable phase-matching conditions [40–43].

There has been growing interest in studying HHG driven by vector [44,45], vortex [46–48], vector-vortex [49], and circularly polarized beams [50–52]. To produce high-brightness harmonic radiation with complex polarization states, it is critical to understand the phase-matching conditions, especially when using longer wavelength driving beams to reach shorter wavelengths. However, polarization studies to date have largely been limited to NIR and optical wavelengths.

In this work, we present experimental results of HHG using a 1300 nanometer (nm) driving beam in three different polarization states: linear, radial, and azimuthal. We found that the optimal phase-matching pressure differed by a factor of two between the linear and vector polarized driving beams. We attribute the difference in pressure to the Guoy phase term in the phase-matching equation, which is two times larger for the vector beam than for the linear beam. We use 3D-printed gas cells designed to optimize the pressure profile in the interaction. We provide characterization and validation of this technique through flow simulations and experimental results.

2. METHODS

The experiment was performed with the output of an optical parametric amplifier (OPA, Light Conversion TOPAS-Prime) driven by a Ti:sapphire laser system (Spectra Physics Solstice ACE). With a central wavelength of 1300 nm, a pulse duration of 35 femtoseconds (fs) and a pulse energy up to 1 milliJoule (mJ), the linearly polarized beam was focused to intensities of $1.9 \pm 0.4 \times 10^{14}$ W/cm^2 using an anti-reflection (AR) coated lens with a focal length of 200 millimeters (mm). The focal spot size was inferred from a measurement of the second-harmonic signal focal spot. With a beam radius of $w_0 = 37.8 \pm 3$ micrometers (μm), the Rayleigh length was calculated to be $z_R = 3.3 \pm 0.3$ mm. The experimental configuration to create the vector beams was identical, except for a half-waveplate (HWP) and an "S-waveplate" (SWP) [53] that were placed before the lens. The HWP was used to set the angle of the incident polarization angle relative to the axis of the SWP. This determines if the output polarization state is radial, azimuthal, or a superposition of the two. In the configuration with the SWP, the energy of the input beam was increased by a factor of 2.79 to maintain the same peak intensity as the linearly polarized beam. A simplified diagram of the experimental setup is shown in Fig. 1.

The laser was focused into a 3D-printed gas cell filled with argon, designed to provide a uniform density profile. The cell was fabricated from a Stratasys Objet260 Connex3 machine using VeroClear material. The entry and exit orifices of the cell are 500 μm in diameter, and the length of the interaction region was 2.5 mm. The gas cell was positioned at the focal plane of the laser with an estimated uncertainty of ±1 mm due to manual alignment of the visible plasma channel. This corresponds to ∼30% of the Rayleigh length, where the on-axis intensity remains within 10% of its peak value. Small adjustments to the gas cell position (within 100 μm) optimized the peak of a single harmonic and increased the overall flux of the measured spectrum. Larger steps decreased the overall flux and shifted the center of the spectrum. The backing pressure was varied during the experiment between 50 and 550 Torr. Differential pumping isolated the flow out of the gas cell from the remaining vacuum system.

The output radiation produced in the gas cell was characterized in both its spectral content and spatial profile. The harmonic radiation was isolated from the fundamental driving wavelengths using ultrathin x-ray filters made of aluminum, zirconium, or a combination of the two, depending on the diagnostic used. These materials are opaque to the fundamental wavelength but transmit EUV wavelengths. The harmonic spectra were measured with a home-built flat-field spectrometer [54], which used a variable line spacing imaging grating (Hitachi, 1200 lines/mm) [55]. Time-integrated spectra were measured *in situ* with an x-ray CCD (Andor-Newton). The spatial profile of the harmonic radiation was measured by placing the x-ray CCD directly in the filtered beam path, rather than at the output of the spectrometer.

3. RESULTS

The harmonic radiation through 400 nm of zirconium is plotted as a function of pressure in Fig. 2. For each of the polarization states measured, there is a well-defined maxima in the normalized flux that can be observed in both the wavelength and the backing pressure. Considering only the spectral axis, the signal decays (rather than plateauing) on both sides of this peak for the same wavelengths for all polarization states. The spectral peak is at ∼14.6 nm and remained relatively constant as the pressure was varied. Along the pressure axis, there is a similar peak and decay in the normalized flux. The pressure peak for the radial polarization case (346 Torr) is approximately the same as the peak for the azimuthal polarization case (376 Torr), both of which are roughly twice the peak found for the linear polarization case (165 Torr).

The entire spatial profile of the harmonic radiation was captured with the x-ray CCD (see Fig. 3). In order to isolate a narrow spectral window, both aluminum and zirconium filters were used to provide a bandpass of 17–20 nm. The linearly polarized driving beam generated harmonic radiation with a Gaussian spatial profile, whereas for the vector beams, the generated harmonic radiation was ring-shaped. Example profiles for the linear and radial polarization drivers are shown in Fig. 3. The harmonic flux is comparable between the two polarization states.

4. DISCUSSION

The peak in the pressure scan for each polarization state indicates that phase-matching conditions are being met. We can write the phase-matching equation as

$$\Delta k \approx P \left[\underbrace{-\frac{\eta \lambda_0 r_e}{k_B T}\left(q - \frac{1}{q}\right)}_{\Delta k_{\text{plasma}}} + \underbrace{\frac{2\pi q(1-\eta)\Delta n}{\lambda_0 k_B T N_{1\,\text{atm}}}}_{\Delta k_{\text{neutral}}} \right] \underbrace{-\frac{q\pi D^2}{4\lambda_0 f^2}}_{\Delta k_{\text{Gouy}}}, \tag{1}$$

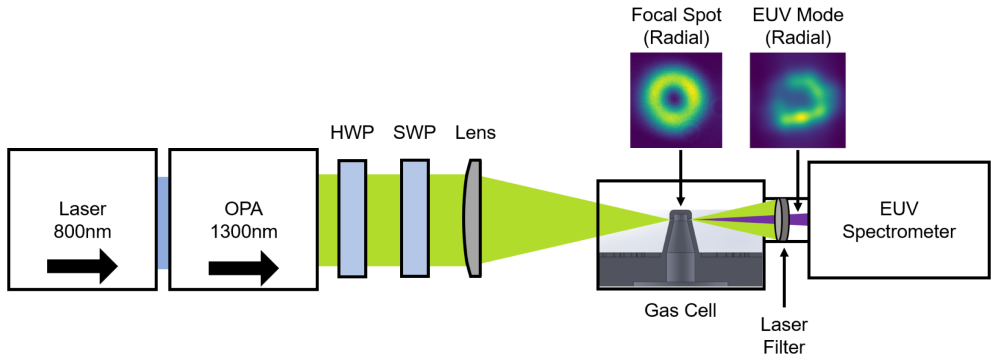

Fig. 1. Experimental setup showing the "S" waveplate that creates the vector polarization states, which are then focused into the gas cell, where high harmonics are generated. The laser light is filtered out so that the harmonics can be measured with the EUV spectrometer.

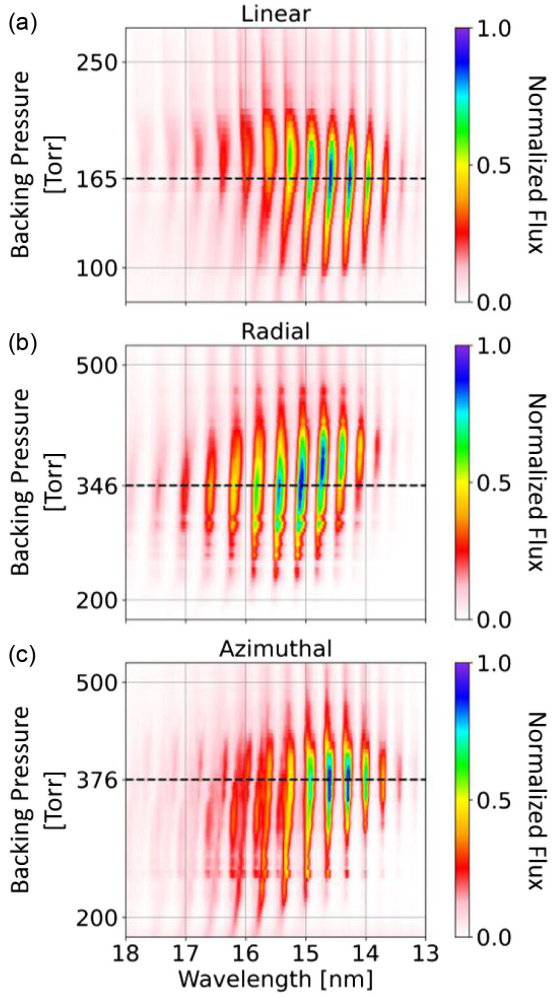

Fig. 2. EUV spectra measured at individual pressures, then binned, stacked, and interpolated to plot on linear axes. Pressure scans were performed with a 1300 nm driving beam of linear (top row), radial (middle row), and azimuthal (bottom row) polarizations. Dashed lines mark the pressure at the peak flux. Spectra were taken with zirconium filters with a total thickness of 400 nm.

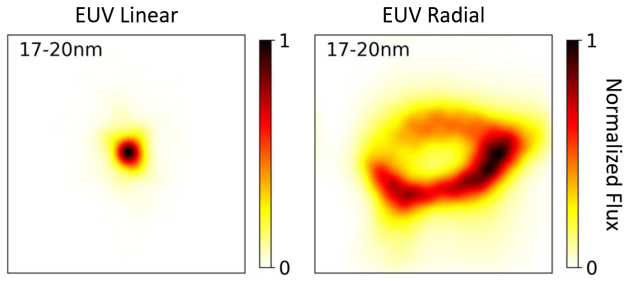

Fig. 3. Direct measurements of the EUV light produced by both the linear and vector polarized driving beams. High frequency components of the measured signal, such as the mesh grid of the ultrathin filters, were removed using a Fourier filter.

where the gas pressure, P, has been factored out of the plasma and neutral dispersion terms, η is the fractional ionization level, λ_0 is the laser wavelength, r_e is the classical electron radius, k_B is the Boltzmann constant, T is the temperature, q is the harmonic order, Δn is the difference in the index of refraction between the fundamental beam and the harmonic beam, $N_{1\,\mathrm{atm}}$ is the gas density at atmospheric pressure, D is the beam diameter, f is the focal length, and the intrinsic phase has been neglected. This assumption is valid when the target is near focus ($z = 0$) in long focal length geometries that satisfy the paraxial approximation. The divergence half-angle in our geometry is $\theta = \arctan(D/2f) = 0.63°$, which satisfies this condition. The same approach was used in studies performed in similar pressure ranges [40,41]. We are also assuming a free-focusing geometry such that the phase mismatch due to geometry may be described with the Gouy phase. If all variables are fixed and only the pressure is changed, Δk varies linearly and intercepts 0 when the expression in the bracket on the right-hand side of Eq. (1) is equal to the Gouy phase term. This pressure-tuning phasematching [29,30] resulted in the peak at 165 Torr for the linear polarization state [Fig. 2(a)]. The peak along the spectral axis at 14.6 nm is also an indication of phase matching. The optimal phase-matching pressure and wavelength measured with the linear polarization state are consistent with previous phase-matching studies with 1300 nm driving beams [40].

The vector polarization states produce similar peaks along each axis [Figs. 2(b) and 2(c)], indicating that phase-matching conditions are being met in these cases as well. Similar to the linear polarization state, the peak along the spectral axis for both vector polarization states occurs at, or near, 14.6 nm. The location of this peak in spectral space is determined by the wavelength and intensity of the driving

beam [25,26]. The wavelength was 1300 nm for all polarization states; therefore, the peak intensity must have been similar for each case. This can be further supported by a model of the intensity profile for each polarization state in the same focusing geometry. The radially polarized electric field amplitude can be expressed as a combination of Hermite–Gaussian modes: $|u_{\mathrm{Rad}}\rangle = |HG_{10}\rangle\hat{x} + |HG_{01}\rangle\hat{y}$. Similarly, the azimuthally polarized field amplitude can be written as $|u_{\mathrm{Az}}\rangle = |HG_{01}\rangle\hat{x} - |HG_{10}\rangle\hat{y}$. The intensity profile of these two ideal vector beam states is identical. By comparing these profiles to a linearly polarized Gaussian profile, we find that the peak intensity of the linear state is ∼2.7 times greater than the peak intensity of the vector beams. In our experiment, we increased the energy of the vector beams by a factor of 2.79, which agrees with this model.

The observed shift in the optimal phase-matching pressure between the linear and vector polarization states is likely primarily due to the difference in the Gouy phase, Φ_{Gouy}. For a linearly polarized Gaussian beam in a free-focusing geometry, this term varies as $-\arctan(z/z_R)$, where z_R is the Rayleigh length. Near $z = 0$, we can make the approximation $\Phi_{\mathrm{Gouy}} = k_{\mathrm{Gouy}} z \approx -z/z_R$. The phase mismatch, $\Delta k_{\mathrm{Gouy}} = q\,k_{\mathrm{Gouy},\omega_0} - k_{\mathrm{Gouy},q\omega_0}$, is dominated by the fundamental term: $q\,k_{\mathrm{Gouy},\omega_0} = -q/z_R = -q\lambda_0/\pi w_0^2$. Plugging in the expression for the beam waist, $w_0 = 2\lambda_0 f/\pi D$, yields the expression for the Gouy phase term in Eq. (1). By modeling the vector beams as combinations of HG_{10} and HG_{01} modes, we find that the Gouy phase for both the radial and azimuthal polarization states is $-2\arctan(z/z_R)$. This doubling of the Gouy phase was experimentally verified for radially polarized beams in 2016 by Kaltenecker *et al.* [56]. Equation (1) describes the phase mismatch for the linear polarization state. We can write out the equivalent equation for the vector polarization states and set each equal to zero. We can solve for the optimal phase-matching pressure of the vector polarization states, P_{VP}, in terms of that for the linear polarization state, P_{LP}. Because the intensity is the same for all cases, the expression in the brackets is unchanged. Since the relationship between the Gouy phase terms is $\Delta k_{\mathrm{Gouy,VP}} = 2\Delta k_{\mathrm{Gouy,LP}}$, then, in the approximation that the intrinsic phase is negligible, the relationship between the pressures must be $P_{\mathrm{VP}}/P_{\mathrm{LP}} \approx 2$. The ratio, $P_{\mathrm{VP}}/P_{\mathrm{LP}}$, at ∼14.6 nm was measured to be ∼2.1 for the radial polarization, which deviates from the theoretical model by 5%. In the azimuthal polarization state, $P_{\mathrm{VP}}/P_{\mathrm{LP}}$ at the same wavelength was measured to be ∼2.3, which deviates from the theoretical model by 15%.

The observed discrepancies may be due, in part, to the intrinsic phase, which varies as the gradient of the intensity [33–36] and may impact the phase matching in the longitudinal direction. When the target is at the focal plane ($z = 0$ mm), the gradient of the intensity in the longitudinal direction is 0. However, the error bar in our focal plane alignment was ±1 mm. At $z = 1$ mm, the peak intensity of a linearly polarized Gaussian beam decreases by ∼10% (assuming a focal geometry identical to the one used in our experiment). The same is true for the vector polarization states modeled by HG modes. This could result in the longitudinal intrinsic phase becoming significant enough to cause the discrepancies observed in the phase-matching pressure ratios.

The intrinsic phase and other intensity fluctuations may also be responsible for the different trends in the slope of the phase-matching curves in Fig. 2. The linear polarization state produces a curve with a negative slope, whereas the radial and azimuthal polarization states produce curves with positive slopes (of different magnitudes). It is possible that imperfections in the driving beam intensity profile could cause variations in the intrinsic phase for a particular harmonic order, which could change the optimal phase-matching pressure for that order. These imperfections could have been introduced by the nonlinear processes in the OPA. Alternatively, it is possible that the S-waveplate could introduce polarization or mode defects if the incidence angle is not perfectly normal. Theoretically, the radial and azimuthal polarization states should be identical, but asymmetry in either beam profile could have caused the difference in slope between the two states.

The direct measurement of the harmonic radiation produced by the radially polarized beam [Fig. 3(b)] confirms that the ring-shaped mode is preserved in the interaction. While the polarization was not directly measured, Hernández-García *et al.* confirmed that HHG with a gas target imprints both radial and azimuthal polarization states from the driving beam to the harmonic radiation [44]. Studies with more complex polarization states also confirmed that polarization is preserved in the HHG interaction [45,49]. However, all these studies were performed at shorter wavelengths, limiting the harmonic order q to a maximum of ∼27. With longer wavelength driving beams, both the maximum energy and the harmonic order q increase substantially. For instance, in the 17–20 nm spectral range transmitted by the x-ray filters in our experiment, harmonic orders from the 65th to the 75th were measured. At such high orders, the divergence of harmonic radiation is nearly identical between orders, leading to spatial overlap. The observation of a well-defined ring structure at these high harmonic orders indicates that the vector polarization state is preserved in the interaction. As the harmonic order increases, the impact from mode imperfections also increases, as the interference between each mode accumulates. These imperfections could contribute to the transverse intrinsic phase, which could affect the divergence and structure of the EUV profile. Improving the driving beam mode quality would likely increase conversion efficiency and harmonic mode quality.

Our phase-matching measurements were enabled by the 3D-printed gas cell. The gas cell provides a cost-effective, customizable alternative to simple gas jets. It consists of a gas-filled interaction region with entrance and exit orifices for the laser to pass through. The free-focusing geometry, similar to a gas jet, enabled the vector polarization states to propagate freely through the interaction region. Because there is no optical guiding, the mode is preserved in the interaction, enabling us to create harmonic radiation with vector polarization states.

Our phase-matching model assumes that the gas cell creates a confined region of uniform pressure, an assumption we validate through numerical simulations and experimental measurements. We modeled the gas density profile using SolidWorks Flow Simulation, a CAD-embedded computational fluid dynamics (CFD) tool that solves the complete Navier–Stokes equations. The results show that the pressure remains very uniform (within 0.05%) throughout the interaction region and

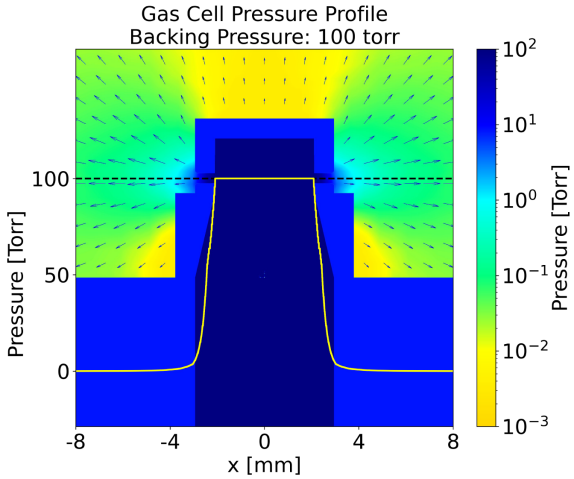

Fig. 4. Flow simulation of the gas cell shows an interaction pressure nearly identical to the backing pressure of 100 Torr. The color bar (log scale) indicates the pressure in the image. The arrows in the image represent the direction of the gas flow. A lineout along the dotted black line is overlaid on the image (yellow).

drops off rapidly within the orifices (see Fig. 4). The simulations also show that a backing pressure of 100 Torr yields a nearly identical interaction pressure of 99.73 Torr. Using the gas cell and a linearly polarized 800 nm driving beam, we experimentally measured an optimal phase-matching pressure of 70 Torr with peak flux at a wavelength of 27.6 nm, which agrees with previous studies [57].

Using the 3D-printed gas cell as the target in our experiment was an integral component in obtaining these results. High-pressure gas jets inherently produce a non-uniform density profile, making them less ideal for phase-matching studies. Additionally, the vacuum system can only accommodate a certain amount of gas flow. The use of gas cells to confine the gas enables much lower flows than a gas jet. Even though the optimal phase-matching pressure for the vector polarization states was roughly twice that of the linear polarization state, this regime was accessible because of the gas cell. Using 3D-printed gas cells rather than traditional gas cells enabled rapid prototyping to optimize the measured HHG flux. Design flexibility was limited with the traditional gas cells available, making it difficult to generate harmonic spectra with a high signal-to-noise ratio.

5. CONCLUSION

We have shown experimental results of phase-matched HHG in a 3D-printed gas cell using a 1300 nm driving beam in linear and vector polarization states. The spatial profiles of the EUV light match those of the corresponding driving beams, confirming spatial mode transfer. Maintaining the same experimental parameters for each polarization state and varying only the backing pressure, we found that the optimal phase-matching pressure was roughly two times higher for the vector polarization states than the linear state. We believe that this is primarily a consequence of the spatial mode of the vector beams that doubles the Gouy phase and not a polarization-dependent phenomenon. This work was enabled by 3D-printed gas cells that create a confined region of uniform pressure conducive to phase matching. The phase-matching conditions for the vector polarization states were achievable because the gas cell preserved the mode of the driving beam and provided an interaction pressure nearly identical to the backing pressure.

Our findings suggest that it may be useful to further explore phase-matching conditions for vortex driving beams in HHG. While these beams carry a unique phase structure, the ring-shaped intensity profile is very similar to the vector beams used in our experiment. The 3D-printed gas cell facilitates HHG with such unconventional spatial modes and supports alternative geometries such as noncollinear setups and variable-length designs. The low cost and design flexibility of the gas cells provide exciting opportunities for experimental prototyping and customized targetry in HHG.

Funding. National Science Foundation (DMR-1548924, PHY-1753165, PHY-1903709).

Disclosures. The authors declare no conflicts of interest.

Data availability. Data underlying the results presented in this paper are not publicly available at this time but may be obtained from the authors upon reasonable request.

REFERENCES

1. R. Dorn, S. Quabis, and G. Leuchs, "Sharper focus for a radially polarized light beam," Phys. Rev. Lett. **91**, 233901 (2003).
2. G. Milione, M. P. J. Lavery, H. Huang, *et al.*, "4 × 20 Gbit/s mode division multiplexing over free space using vector modes and a q-plate mode (de)multiplexer," Opt. Lett. **40**, 1980–1983 (2015).
3. G. Milione, T. A. Nguyen, J. Leach, *et al.*, "Using the nonseparability of vector beams to encode information for optical communication," Opt. Lett. **40**, 4887–4890 (2015).
4. Y. Zhao and J. Wang, "High-base vector beam encoding/decoding for visible-light communications," Opt. Lett. **40**, 4843–4846 (2015).
5. Z. Zhu, M. Janasik, A. Fyffe, *et al.*, "Compensation-free high-dimensional free-space optical communication using turbulence-resilient vector beams," Nat. Commun. **12**, 1666 (2021).
6. P. Török and P. Munro, "The use of Gauss-Laguerre vector beams in STED microscopy," Opt. Express **12**, 3605–3617 (2004).
7. R. Chen, K. Agarwal, C. J. R. Sheppard, *et al.*, "Imaging using cylindrical vector beams in a high-numerical-aperture microscopy system," Opt. Lett. **38**, 3111–3114 (2013).
8. Z. Rong, C. Kuang, Y. Fang, *et al.*, "Super-resolution microscopy based on fluorescence emission difference of cylindrical vector beams," Opt. Commun. **354**, 71–78 (2015).
9. Q. Zhan, "Trapping metallic Rayleigh particles with radial polarization," Opt. Express **12**, 3377–3382 (2004).
10. S. Yan and B. Yao, "Radiation forces of a highly focused radially polarized beam on spherical particles," Phys. Rev. A **76**, 053836 (2007).
11. M. Michihata, T. Hayashi, and Y. Takaya, "Measurement of axial and transverse trapping stiffness of optical tweezers in air using a radially polarized beam," Appl. Opt. **48**, 6143–6151 (2009).
12. Y. Kozawa and S. Sato, "Optical trapping of micrometer-sized dielectric particles by cylindrical vector beams," Opt. Express **18**, 10828–10833 (2010).
13. N. Bhebhe, P. A. C. Williams, C. Rosales-Guzmán, *et al.*, "A vector holographic optical trap," Sci. Rep. **8**, 17387 (2018).
14. C. Hnatovsky, V. Shvedov, W. Krolikowski, *et al.*, "Revealing local field structure of focused ultrashort pulses," Phys. Rev. Lett. **106**, 123901 (2011).
15. Y. Jin, O. J. Allegre, W. Perrie, *et al.*, "Dynamic modulation of spatially structured polarization fields for real-time control of ultrafast laser-material interactions," Opt. Express **21**, 25333–25343 (2013).
16. J. Ouyang, W. Perrie, O. J. Allegre, *et al.*, "Tailored optical vector fields for ultrashort-pulse laser induced complex surface plasmon structuring," Opt. Express **23**, 12562–12572 (2015).

17. E. Skoulas, A. Manousaki, C. Fotakis, *et al.*, "Biomimetic surface structuring using cylindrical vector femtosecond laser beams," Sci. Rep. **7**, 45114 (2017).
18. M. Blanco, F. Cambronero, M. T. Flores-Arias, *et al.*, "Ultraintense femtosecond magnetic nanoprobes induced by azimuthally polarized laser beams," ACS Photonics **6**, 38–42 (2019).
19. H. Fujita and M. Sato, "Nonequilibrium magnetic oscillation with cylindrical vector beams," Sci. Rep. **8**, 15738 (2018).
20. Y. I. Salamin, Z. Harman, and C. H. Keitel, "Direct high-power laser acceleration of ions for medical applications," Phys. Rev. Lett. **100**, 155004 (2008).
21. V. Marceau, C. Varin, T. Brabec, *et al.*, "Femtosecond 240-keV electron pulses from direct laser acceleration in a low-density gas," Phys. Rev. Lett. **111**, 224801 (2013).
22. A. l'Huillier, L. A. Lompre, G. Mainfray, *et al.*, "Multiply charged ions induced by multiphoton absorption in rare gases at 0.53 μm," Phys. Rev. A **27**, 2503–2512 (1983).
23. M. Hentschel, R. Kienberger, C. Spielmann, *et al.*, "Attosecond metrology," Nature **414**, 509–513 (2001).
24. P. M. Paul, E. S. Toma, P. Breger, *et al.*, "Observation of a train of attosecond pulses from high harmonic generation," Science **292**, 1689–1692 (2001).
25. P. B. Corkum, "Plasma perspective on strong field multiphoton ionization," Phys. Rev. Lett. **71**, 1994–1997 (1993).
26. M. Lewenstein, P. Balcou, M. Y. Ivanov, *et al.*, "Theory of high-harmonic generation by low-frequency laser fields," Phys. Rev. A **49**, 2117–2132 (1994).
27. B. Shan and Z. Chang, "Dramatic extension of the high-order harmonic cutoff by using a long-wavelength driving field," Phys. Rev. A **65**, 011804 (2001).
28. J. Tate, T. Auguste, H. G. Muller, *et al.*, "Scaling of wave-packet dynamics in an intense midinfrared field," Phys. Rev. Lett. **98**, 013901 (2007).
29. A. Rundquist, C. G. Durfee, Z. Chang, *et al.*, "Phase-matched generation of coherent soft x-rays," Science **280**, 1412–1415 (1998).
30. C. G. Durfee, A. R. Rundquist, S. Backus, *et al.*, "Phase matching of high-order harmonics in hollow waveguides," Phys. Rev. Lett. **83**, 2187–2190 (1999).
31. A. L'Huillier, X. F. Li, and L. A. Lompré, "Propagation effects in high-order harmonic generation in rare gases," J. Opt. Soc. Am. B **7**, 527–536 (1990).
32. P. Balcou and A. L'Huillier, "Phase-matching effects in strong-field harmonic generation," Phys. Rev. A **47**, 1447–1459 (1993).
33. P. Saliéres, A. L'Huillier, and M. Lewenstein, "Coherence control of high-order harmonics," Phys. Rev. Lett. **74**, 3776–3779 (1995).
34. J. Peatross, M. V. Fedorov, and K. C. Kulander, "Intensity-dependent phase-matching effects in harmonic generation," J. Opt. Soc. Am. B **12**, 863–870 (1995).
35. M. Lewenstein, P. Saliéres, and A. L'Huillier, "Phase of the atomic polarization in high-order harmonic generation," Phys. Rev. A **52**, 4747–4754 (1995).
36. P. Balcou, P. Saliéres, A. L'Huillier, *et al.*, "Generalized phase-matching conditions for high harmonics: the role of field-gradient forces," Phys. Rev. A **55**, 3204–3210 (1997).
37. A. L'Huillier, K. J. Schafer, and K. C. Kulander, "Theoretical aspects of intense field harmonic generation," J. Phys. B **24**, 3315–3341 (1991).
38. A. L'Huillier, M. Lewenstein, P. Saliéres, *et al.*, "High-order harmonic-generation cutoff," Phys. Rev. A **48**, R3433–R3436 (1993).
39. V. T. Platonenko and V. V. Strelkov, "Generation of high-order harmonics in a high-intensity laser radiation field," Quantum Electron. **28**, 564–583 (1998).
40. T. Popmintchev, M.-C. Chen, O. Cohen, *et al.*, "Extended phase matching of high harmonics driven by mid-infrared light," Opt. Lett. **33**, 2128–2130 (2008).
41. T. Popmintchev, M.-C. Chen, A. Bahabad, *et al.*, "Phase matching of high harmonic generation in the soft and hard X-ray regions of the spectrum," Proc. Natl. Acad. Sci. USA **106**, 10516–10521 (2009).
42. M.-C. Chen, P. Arpin, T. Popmintchev, *et al.*, "Bright, coherent, ultrafast soft x-ray harmonics spanning the water window from a tabletop light source," Phys. Rev. Lett. **105**, 173901 (2010).
43. T. Popmintchev, M.-C. Chen, D. Popmintchev, *et al.*, "Bright coherent ultrahigh harmonics in the keV x-ray regime from mid-infrared femtosecond lasers," Science **336**, 1287–1291 (2012).
44. C. Hernández-García, A. Turpin, J. San Román, *et al.*, "Extreme ultraviolet vector beams driven by infrared lasers," Optica **4**, 520–526 (2017).
45. F. Kong, C. Zhang, H. Larocque, *et al.*, "Vectorizing the spatial structure of high-harmonic radiation from gas," Nat. Commun. **10**, 2020 (2019).
46. M. Zürch, C. Kern, P. Hansinger, *et al.*, "Strong-field physics with singular light beams," Nat. Phys. **8**, 743–746 (2012).
47. G. Gariepy, J. Leach, K. T. Kim, *et al.*, "Creating high-harmonic beams with controlled orbital angular momentum," Phys. Rev. Lett. **113**, 153901 (2014).
48. F. Kong, C. Zhang, F. Bouchard, *et al.*, "Controlling the orbital angular momentum of high harmonic vortices," Nat. Commun. **8**, 14970 (2017).
49. A. de las Heras, A. K. Pandey, J. San Román, *et al.*, "Extreme-ultraviolet vector-vortex beams from high harmonic generation," Optica **9**, 71–79 (2022).
50. D. D. Hickstein, F. J. Dollar, P. Grychtol, *et al.*, "Non-collinear generation of angularly isolated circularly polarized high harmonics," Nat. Photonics **9**, 743–750 (2015).
51. P.-C. Huang, C. Hernández-García, J.-T. Huang, *et al.*, "Polarization control of isolated high-harmonic pulses," Nat. Photonics **12**, 349–354 (2018).
52. K. M. Dorney, L. Rego, N. J. Brooks, *et al.*, "Controlling the polarization and vortex charge of attosecond high-harmonic beams via simultaneous spin–orbit momentum conservation," Nat. Photonics **13**, 123–130 (2019).
53. M. Beresna, M. Gecevičius, P. G. Kazansky, *et al.*, "Radially polarized optical vortex converter created by femtosecond laser nanostructuring of glass," Appl. Phys. Lett. **98**, 201101 (2011).
54. D. Neely, D. Chambers, C. Danson, *et al.*, "A multi-channel soft x-ray flat-field spectrometer," AIP Conf. Proc. **426**, 479–484 (1998).
55. T. Kita, T. Harada, N. Nakano, *et al.*, "Mechanically ruled aberration-corrected concave gratings for a flat-field grazing-incidence spectrograph," Appl. Opt. **22**, 512–513 (1983).
56. K. J. Kaltenecker, J. C. König-Otto, M. Mittendorff, *et al.*, "Gouy phase shift of a tightly focused, radially polarized beam," Optica **3**, 35–41 (2016).
57. M.-C. Chen, "Modifying driving laser wavelength to generate coherent, ultrafast x-rays from phase-matched high-order harmonics," Ph.D. thesis (University of Colorado, 2012).